Title

Spin Chains with Highly Quantum Character through Strong Covalency in Ca_3CrN_3

Journal

Journal of the American Chemical Society, 147(4)

ISSN

0002-7863 1520-5126

Authors

Kautzsch, Linus

Georgescu, Alexandru B

Yuan, Lin-Ding

et al.

Publication Date

2025-01-21

DOI

10.1021/jacs.4c11629

Peer reviewed

Spin Chains with Highly Quantum Character through Strong Covalency in Ca_3CrN_3

Linus Kautzsch,[*,†] Alexandru B. Georgescu,[*,‡] Lin-Ding Yuan,[‡] Keith M. Taddei,[§] Aiden Reilly,[†] Ram Seshadri,[†] James M. Rondinelli,[*,‡] and Stephen D. Wilson[*,⊥]

†*Materials Department and Materials Research Laboratory*

University of California, Santa Barbara, Santa Barbara, CA, 93106, United States

‡*Department of Materials Science and Engineering*

Northwestern University, Evanston, Illinois, 60208, United States

¶*Department of Chemistry, Indiana University, Bloomington, Indiana 47405, United States*

§*Neutron Scattering Division, Oak Ridge National Laboratory*

Oak Ridge, TN, 37831, United States

‖*Department of Chemistry and Biochemistry*

University of California, Santa Barbara, Santa Barbara, CA, 93106, United States

⊥*Materials Department*

University of California, Santa Barbara, Santa Barbara, CA, 93106, United States

E-mail: kautzsch@ucsb.edu; georgesc@iu.edu; jrondinelli@northwestern.edu; stephendwilson@ucsb.edu

Abstract

The insulating transition metal nitride Ca_3CrN_3 consists of sheets of triangular $[CrN_3]^{6-}$ units with C_{2v} symmetry that are connected via quasi-1D zig-zag chains. Due to strong covalency between Cr and N, Cr^{3+} ions are unusually low-spin, and $S = 1/2$. Magnetic susceptibility measurements reveal dominant quasi-1D spin correlations with very large nearest-neighbor antiferromagnetic exchange $J = 340\,\mathrm{K}$ and yet no sign of magnetic order down to $T = 0.1\,\mathrm{K}$. Density functional theory calculations are used to model the local electronic structure and the magnetic interactions, supporting the low-spin assignment of Cr^{3+} that is driven by strong π donation from the nitride ligands. The surprising failure of interchain exchange to drive long-range magnetic order is accounted for by the complex connectivity of the spin chain pairs that further frustrates order. Our combined results establish Ca_3CrN_3 as a nearly ideal manifestation of a quantum spin chain whose dynamics remain unquenched down to extraordinarily low temperatures despite strong near-neighbor exchange coupling.

Introduction

The discovery of new magnetic materials is of key importance to multiple fields, with applications ranging from the discovery of ferromagnets for wind power and electric vehicles, magnetoresistive materials for microelectronics and memory devices, and novel materials for spintronic and quantum information applications. Many of the most well-studied magnetic materials are transition metal oxide perovskites[1] and spinels,[2] owing to the wide array of possible stoichiometries, doping, layering, and tunable magnetic ordering temperatures. Ternary oxides without octahedral building units hosting the magnetic ions have also recently gained interest for quantum information science applications, including spin-chain materials.[3,4] Recent investigations have also focused on 2D halides,[5] van der Waals materials,[6] as well as heteroanionic oxyhalides and oxyfluorides.[7]

Less explored are ternary magnetic nitrides, despite renewed interest in ternary main group nitride semiconductors, e.g., $CaSnN_2$,[8] $MgSnN_2$,[9] $CaGaN_5$,[10] and Li_3AlN_2.[11] Ternary nitrides with transition metals have been synthesized using bulk synthetic methods (e.g. $MgZrN_2$[12] and CaNiN[13]), using high-pressure techniques (e.g. Pr_2ReN_4, Nd_2ReN_4 and Ce_2TaN_4[14]), and as thin films (e.g. $MgTiN_2$,[15] $ZnMoN_2$,[16] $ZnZrN_2$[17] and $LaWN_3$,[18]). Compounds in this class with unquenched local moments are rare, but when they do exist, they often exhibit complex magnetism. For example the frustrated spinel $MnTa_2N_4$ exhibits helicoidal and spin-glass behavior[19] while the noncollinear antiferromagnet $MnSiN_2$ exhibits spin canting and polar order[20]—both arising from the tetrahedral MnN_4 units and their connectivity with other motifs to form an extended structure. Owing to the tendency for nitrido anions to form multiple bonds, exhibiting both σ and π bonding interactions,[21] metal-rich ternary nitrides exhibit unique structures, such as Sr_3CrN_3,[22] Ca_6FeN_5,[23] and Ca_3CrN_3,[24] with uncommon and low transition metal coordination environments and spin states.[25,26]

Although hexagonal Sr_3CrN_3 is a reported electride with nonmagnetic Cr sites,[22] replacing the alkali metal with Ca leads to an orthorhombic structure and a local moment forms on the Cr site. This was first reported by Vennos et al.,[24] demonstrating that Ca_3CrN_3 hosts Cr^{3+}

ions in a planar triangular coordination of ligands. More recently, Cao et al. demonstrated a reversible topochemical transformation of the orthorhombic Ca_3CrN_3 into a hexagonal antiperovskite phase Ca_3CrN_3H upon dehydrogenation/hydrogenation[27] and identified the nitride-hydride compound as a promising catalyst for ammonia synthesis.[28] Without hydride incorporation, which occurs for syntheses in a hydrogen atmosphere at temperatures above 670 K,[27] Ca_3CrN_3 represents the first solid-state example of Cr^{3+} ions in a low-spin ($S = 1/2$) state.

The structure comprises planar $[CrN_3]^{6-}$ triangular units arranged in sheets and oriented in the same direction within the *ab*-plane, stacked along the *c*-axis, and with divalent Ca ions interspersed isolating the triangles. While the Cr-Cr distances are 4.73 Å, suggesting an overall weak magnetic exchange coupling between ions, a high-temperature, broad maximum in the magnetic susceptibility data was reported for Ca_3CrN_3,[24] indicative of short-ranged antiferromagnetic exchange interactions in reduced dimensions. This feature matches the expected susceptibility behavior of a $S = 1/2$ one-dimensional (1D) Heisenberg spin chain;[29] however the exchange pathways generating this behavior and the mechanism for the dimensional confinement of the $S = 1/2$ Cr moments remain open questions.

Formally, long-range order is precluded from forming along Heisenberg $S = 1/2$ antiferromagnetic spin chains in lieu of spinon fluctuations; however, in real materials, $S = 1/2$ spin chains regularly exhibit long-range magnetic order at low temperatures (T_{AF}) due to interchain magnetic exchange pathways and anisotropies that stabilize order.[30,31] Specifically, as nearest neighbor (intrachain) antiferromagnetic exchange increases relative to competing effects, the gapless spin liquid quantum ground state of the $S = 1/2$ 1D antiferromagnetic (AFM) model[32] can be approached more closely—we dub these instances as highly quantum spin chains. In this regime, the fractionalized dynamics of the spin liquid state can drive a host of unusual phenomena.[33–36] The potential for enhanced magnetic exchange interactions in magnetic nitrides is a promising way of accessing this quantum regime in real materials, and, while AFM spin chains are well studied in oxides,[37] they have yet to be extensively

studied in nitrides.

Here we examine the magnetic and electronic properties of Ca_3CrN_3 down to low temperatures to assess whether it embodies the necessary ingredients for quantum magnetism: strong intrachain interactions, weak effective interchain interactions, and low-dimensionality with $S = 1/2$ ions. We employ a combination of AC susceptibility measurements, powder neutron diffraction studies, and electronic structure calculations to interrogate the ground state of this compound, and our results confirm that Cr^{3+} adopts a low-spin configuration and neither shows long-range magnetic order nor spin-freezing down to 100 mK. Our data reveal strong intrachain (J) antiferromagnetic exchange interactions of 340 K, deduced from magnetic susceptibility measurements, which are consistent with our density functional theory calculations that also find a weakly dispersing "flat" valence band. A model is presented for the origin of the strong intrachain exchange which involves the strong π bonding character of terminal N^{3-} anions and a Ca-mediated superexchange pathway via quasi-1D zig-zag chains of $[CrN_3]^{6-}$ units. The interchain interactions are weaker and multiple, competing interchain pathways are identified along the complex Cr-Cr network that further frustrate long-range order. The convergence of these features make orthorhombic Ca_3CrN_3 a highly quantum spin chain compound with uncommon Cr^{3+} $S = 1/2$ moments that are quantum fluctuation dominated and an extraordinarily high reported J/T_{AF} ratio, a record for spin chain materials to the best of our knowledge.

Methods

Synthesis of Ca_3CrN_3

Polycrystalline samples of Ca_3CrN_3 were prepared from Ca_3N_2 (Fisher Scientific, 99%) and CrN/Cr_2N (Fisher Scientific, 99%) in a high-temperature reaction. The starting materials were mixed in a Ca:Cr ratio of 3:1, intimately ground and pelletized. The pellets were then wrapped in molybdenum foil (Fisher Scientific) 99.95% and placed in 3/4-inch smooth-bore

316 stainless steel tubing (McMaster-Carr 89785K859). The molybdenum foil prevents reaction of the compound with the steel tube. The tubes were closed using stainless steel end caps (McMaster-Carr 5182K695). These steps were conducted within a glovebox filled with argon, ensuring the samples were sealed in tubes under an argon atmosphere to minimize any hydrogen uptake. The stainless steel tubes were placed in a high-temperature furnace and heated under argon for $t = 96$ h at $T = 1350$ °C. The samples were then slowly cooled at a rate of 60 K/hr to $T = 1050$ °C and subsequently furnace-cooled to room temperature. This procedure resulted in air-sensitive samples with high crystallinity.

Structural Characterization

The sample quality and purity was verified by powder X-ray diffraction (XRD) using a Panalytical Empyrean powder diffractometer operating with Cu-K_α radiation in Bragg-Brentano geometry. Kapton foil was used to prevent air exposure of the samples. Powder neutron diffraction data were collected on the HB-2A beam line at the High Flux Isotope Reactor (HFIR), Oak Ridge National Laboratory. A Ge(113) monochromator and a wavelength of $\lambda = 2.409\,\text{Å}$ was used, and diffraction data were collected at temperatures of 1.5 K, 150 K, and 250 K. Rietveld refinements of the neutron diffraction data were carried out using using the FullProf program.[38] Crystallographic resulting from these refinements are provided in the Supporting Information (SI).

Magnetic Measurements

DC magnetization measurements were performed between $T = 2 - 400$ K using a Quantum Design MPMS3 SQUID vibrating sample magnetometer. Powder with a mass of $m \approx 5$ mg was measured in a polypropylene capsule. DC magnetization data were collected under a constant magnetic field while sweeping temperature at a rate of $7\,\text{K}\,\text{min}^{-1}$. Isothermal magnetization data were collected via five-branch hysteresis loops between $H = -7$ T and $H = 7$ T at $T = 2$ K and at $T = 300$ K using a field ramp rate of 10 mT s^{-1}. AC susceptibility

measurements between $T = 0.1$ K and $T = 4$ K were performed using a Quantum Design 14 T Dynacool physical property measurement system (PPMS) with a ^{3}He/^{4}He dilution refrigerator insert.

First-Principles Calculations

Density functional theory (DFT) calculations were performed using the Quantum Espresso code version 6.7 Max,[39] using the Perdew-Burke-Erzerhof (PBE) exchange-correlation functional,[40,41] including the simplified DFT+U formalism[42] with an applied $U = 2$ eV on the Cr $3d$ manifold. Our planewave DFT simulations employed a 404 eV planewave cutoff, a 5442 eV density cutoff, and were performed with ultrasoft pseudopotentials from the GBRV repository[43] and a total energy convergence criteria of 70 μeV Å^{-1}. We sampled the Brillouin zone using a $5 \times 4 \times 6$ k-point mesh and performed integrations with Gaussian smearing of 0.054 eV. The cell volume and atomic positions were relaxed until the forces were less than 50 meV Å^{-1}. We used a mean-field approach to compute the interchain and intrachain constants. The total energies of different spin configurations were computed, and we mapped these onto a simplified spin Hamiltonian.[44,45] Energetics of the spin configurations are provided in Figures S1-3 of the SI. PBE+U results for $0 \leq U \leq 3$ eV are compared to those obtained from the r^{2}SCAN functional, along with the metaGGA calculations details, in Figure S4 of the SI.

Experimental Results

Crystal structure

Figure 1 shows the crystallographic structures of the cubic nitride Ca_3N_2 and the orthorhombic ternary nitride Ca_3CrN_3. Ca_3N_2 comprises CaN_4 units that form distorted tetrahedra in an edge-sharing network. The structure of Ca_3CrN_3 (Figure 1b) may be related to Ca_3N_2 by introducing Cr^{3+} ions that break up the network into lower dimensional fragments, creating chains of 2×1 rock salt-type CaN cubes along the [001] direction and $[CrN_3]^{6-}$ units in (001)

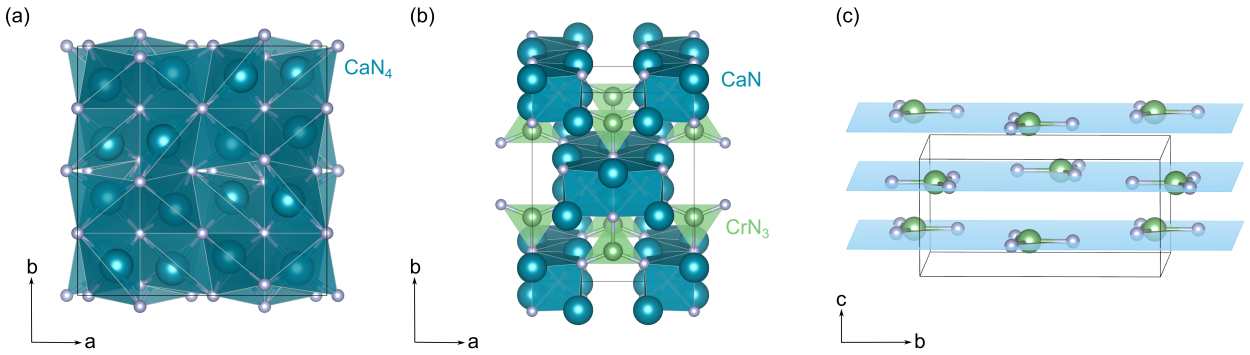

Figure 1: Crystal structures of the cubic nitride Ca_3N_2 (space group $Ia\bar{3}$) and of the orthorhombic nitride Ca_3CrN_3 (space group $Cmcm$). (a) View along the c axis of Ca_3N_2. The structure comprises an edge-sharing network of distorted CaN_4 tetrahedra. (b) View along the c axis of Ca_3CrN_3. 2×1 rock salt-type CaN chains are separated by complex triangular nitridochromate $[CrN_3]^{6-}$ ions. (C) View along the a axis of Ca_3CrN_3 shows the sheet-like nature of the $[CrN_3]^{6-}$ units on (001) planes with ABAB stacking along c.

planes. Alternatively, the CaN_4 tetrahedra in Ca_3N_2 transform into CaN_5 units with square pyramidal coordination and edge-sharing connectivity.

The lower dimensional structure compared to cubic Ca_3N_2, with more directional covalent bonding (Ca-N bonds from 2.44-2.49 Å), leads to a broader distribution of Ca-N bond distances in Ca_3CrN_3 as the alkali earth donates its electrons to the complex nitridochromate fragment. The anionic framework of the nitridometalate comprises isolated planar triangular $[CrN_3]^{6-}$ units with C_{2v} point symmetry, embedded in between the rock salt chains with alternating orientations (ABAB stacking along c). The three nitrido ligands belong to different Wyckoff sites: N1 ($4c$) and N2 ($8g$) in the standard $Cmcm$ setting (space group 63).

The crystal structure of Ca_3CrN_3 was measured via neutron powder diffraction at a variety of temperatures with the data and fits shown in Figure 2. Rietveld analysis performed on neutron diffraction data collected at $T = 1.5$ K reveals that, while the pattern is dominated by the crystallographic reflections of Ca_3CrN_3, traces of Ca_2N (product from the synthesis reaction) and decomposition products that were not immediately present after the synthesis reaction also appear (Figure 2a). We speculate that the sample was exposed to some level of oxygen or moisture during loading into the aluminum sample holder at the beam line. The additional, weak peaks in the pattern can be best attributed to decomposition products CaO

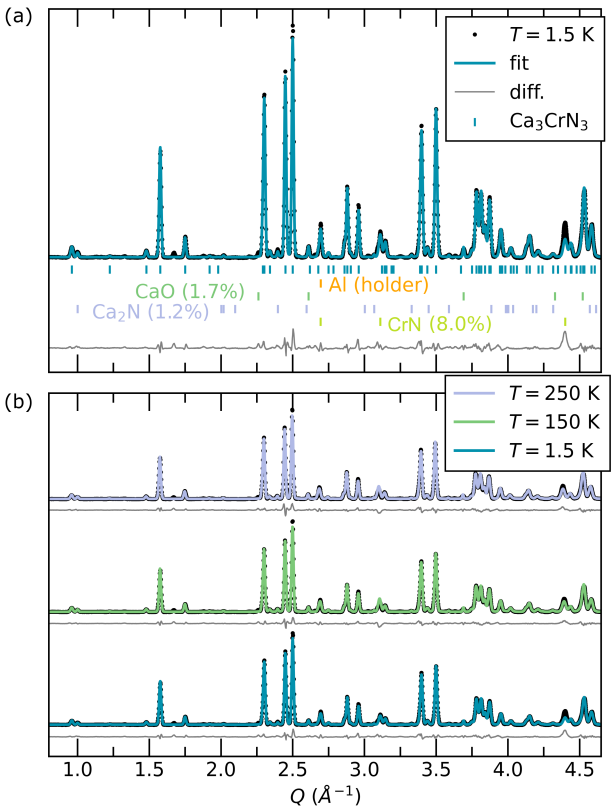

Figure 2: (a) Powder neutron diffraction at $T = 1.5$ K and Rietveld fit including the Ca_3CrN_3 crystallographic phase, Al from the low-temperature sample holder, and the impurities CaO (1.7%), Ca_2N (1.2%), and CrN (8%). (b) Powder neutron diffraction data and Rietveld fits at $T = 250$ K, $T = 150$ K, and $T = 1.5$ K.

(1.7%) and a second, unidentified phase. This second impurity can be modeled as $CrO_{0.87}$ crystallizing in a rock salt defect structure,[46] though the difficulty of synthesizing Cr^{2+} under ambient conditions suggest CrN and other unknown oxynitride phases may instead account for the remaining, weak unindexed peaks in the pattern. Notably, the samples used in the susceptibility measurements discussed later showed no sign of chromium oxide or other oxynitride impurities in powder X-ray diffraction (XRD) measurements.

The 1.5 K refined crystal structure and density functional theory (DFT) relaxed structures are in good agreement. Although the DFT volume is approximately 6 % smaller than the observed structure, the local structure is reproduced well. Both structures exhibit long Cr-N1 and short Cr-N2 bond lengths: 1.86 Å (experiment), 1.76 Å (DFT) and 1.83 Å, 1.76 Å,

respectively, which are shorter than other amido complexes and indicative of the so-called double-faced π-donor character of the nitride ligand.[47,48] (Full structural details are provided in the SI.) This asymmetry distorts the N-Cr-N bond angles away from the ideal equilateral triangle of 120°, leading to N1-Cr-N2 and N2-Cr-N2 bond angles of 112.6, 134.9° (experiment) and 112.1, 135.8° (DFT), respectively. It further leads to a range of Ca-N distances in the structure, varying from 2.38 to 2.72 (experiment) and 2.34 to 2.68 Å (DFT), with the shortest distances between Ca and N1, directed along the *b*-axis. Figure 1c reveals the sheet-like nature of the $[CrN_3]^{6-}$ units along the *c*-axis. Neighboring sheets are displaced by $\frac{1}{2}b$ and rotated in a two-fold fashion around *c*. This creates a zig-zag arrangement of the CrN_3 units along the *c*-axis, and leads to long Cr-Cr distances in the structure, i.e., the shortest Cr-Cr distance is 4.72 Å (experiment) and 4.86 Å (DFT) between layers.

Figure 2b shows the measured neutron diffraction patterns collected at $T = 250$ K, $T = 150$ K, and $T = 1.5$ K and their corresponding Rietveld fits using the above-described phases. The results are shown in Table 1 at all three temperatures, confirming that the neutron data is fully described by the crystallographic phases alone. No significant crystallographic changes are observed between $T = 250$ K and $T = 1.5$ K, except for minor changes in the cell volume from thermal expansion (0.4% in this regime). No additional magnetic peaks appear down to 1.5 K, suggestive of an absence of long-range magnetic order within the typical resolution of powder measurements of $\approx 0.5\ \mu_B$. To investigate the magnetic properties and ground state further, low temperature magnetization measurements were performed.

Magnetic properties

Temperature-dependent magnetic susceptibility measurements reveal a broad feature centered at $T \approx 220$ K and a Curie-like tail at lower temperatures (Figure 3a). The susceptibility data qualitatively resemble that reported by Vennos et al.,[24] which was carried out from $T = 30$ K to 760 K and also showed the onset of Curie tail at low temperatures. In the temperature range explored (below 400 K), we were unable to extract a high-T local moment as Curie-Weiss fits

Table 1: Rietveld refinement data for PND data. Lattice parameters a, b, c, unit cell volume V, and R factors R_{wp} and R_{exp}.

Space group	$Cmcm$		
T (K)	1.5	150	250
a (Å)	8.493	8.498	8.503
b (Å)	10.265	10.272	10.284
c (Å)	5.027	5.029	5.034
α, β, γ (°)	90	90	90
V (Å^3)	438.26	438.99	440.20
$R_{\mathbf{wp}}$	15.6	12.7	10.6
$R_{\mathbf{exp}}$	2.10	2.13	2.17

are only valid in a temperature regime of no or very low spin-spin correlation (Figure 3a); however, earlier measurements up to 700 K extracted a local moment of 1.86 μ_B per Cr.[24]

The broad maximum is often characteristic of low-dimensional spin systems and indicates a crossover from a paramagnetic state into a short-range ordered antiferromagnetic state. The structurally similar $S = 1/2$ 1D spin chain compound $NaCu_2O_2$ exhibits a similarly broad feature centered around $T = 52$ K, for example.[49] As we will show next, the susceptibility data can indeed be modeled using a quasi-1D magnetic framework.

To analyze the broad peak in the magnetic susceptibility, the susceptibility data were fit using the combined contributions from a dilute paramagnetic impurity (χ_{Curie}), a temperature independent Van Vleck term (χ_0), and a Bonner-Fisher type interaction term ($\chi_{1D}(T)$) accounting for short-range spin correlations. The fit form was $\chi(T) = \chi_{Curie}(T) + \chi_0 + \chi_{1D}(T)$. For the Bonner-Fisher term,[50] the polynomial approximation[51,52] was used for the high-temperature spin susceptibility of a quasi-1D spin system with $S = 1/2$ as

$$\chi_{1\mathrm{D}}(T) = \frac{Ng^2\mu_{\mathrm{B}}^2}{k_{\mathrm{B}}T} \frac{0.25 + 0.074965\Gamma + 0.075236\Gamma^2}{1 + 0.9931\Gamma + 0.172135\Gamma^2 + 0.757825\Gamma^3}$$

where N, g, and k_B are the number of spins, the electron g-factor, and Boltzmann constant, respectively, with $\Gamma = J/k_BT$, and $N = N_A$, where N_A is Avogadro's number as there is a single Cr^{3+} ion in the asymmetric unit cell.

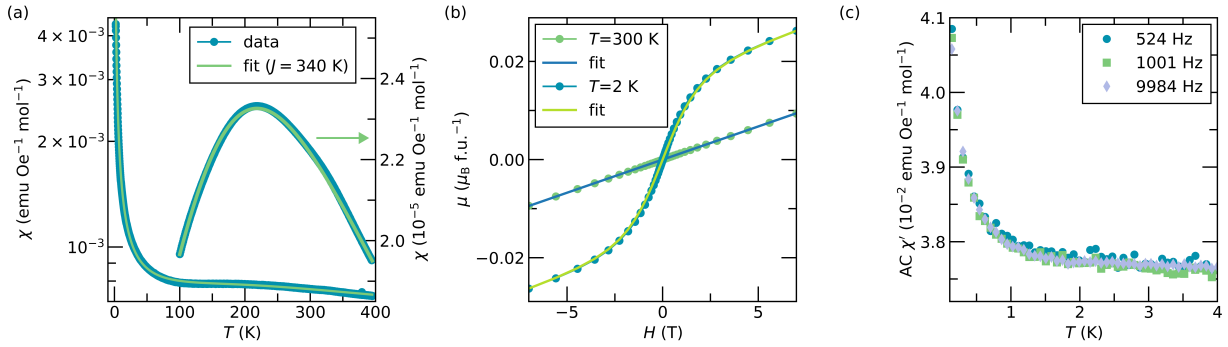

Figure 3: (a) Low-temperature susceptibility measured at an applied field of $H = 0.1$ T showing a Curie tail and a broad anomaly centered around $T = 220$ K. The data was collected using a field-cooled warming (FCW) procedure. A Curie fit allows us to extract the anomaly signal, which is then fit using the Bonner-Fisher model with $J = 340$ K. (b) Magnetic moment μ as a function of the applied magnetic field H at $T = 300$ K and $T = 2$ K. (c) Temperature-dependent real component of the AC susceptibility $\chi'(T)$ under varying AC-drive fields.

The combined fit is shown in Figure 3(a). The low temperature Curie tail fits to a small local moment value of 0.26 μ_B per Cr ion and can be attributed to a small paramagnetic impurity fraction, either within the starting reagents or trace contamination from the molybdenum foil used during the synthesis. The temperature-independent Van Vleck term fits to $\chi_0 = 5.1 \times 10^{-4}$ emu mole^{-1} Oe^{-1} and the χ_{1D} term reveals a large intrachain exchange constant of $J = 340$ K. The χ_0 Van Vleck term is reasonably large for an insulator but not without precedent in small gap compounds such as $NaRuO_2$[53] and of the same order as some larger gap compounds such as Cr_2O_3[54] and V_2O_3.[55]

To better illustrate the χ_{1D} contribution to the data, the small impurity Curie contribution was subtracted from the data and the peak region is overplotted in Figure 3(a). It is worth noting that this fit does not account for multiple extended or competing exchange pathways along or between the chains. Instead, the obtained J value represents a minimal parameterization of the strength of nearest neighbor magnetic interactions leading to the low-dimensional, short-range correlations. The physical description of the exchange pathway mediating this J is discussed below. Alternative models of the peak in $\chi(T)$ based on single-ion effects such as interconfiguration valence fluctuations born from a fluctuating

spin-state transition fail to describe the data.[56] Given the Cr-Cr distance, the extracted exchange coupling is quite large compared to other known oxide spin chains with $S = 1/2$ and comparable cation separations, such as $BaCo_2V_2O_8$ with $J = 65$ K[57] and $NaCu_2O_2$ with $J = 85$ K.[49]

Looking further at the magnetic behavior of Ca_3CrN_3, Figure 3b shows the isothermal magnetization at a variety of temperatures. The linear response at $T = 300$ K evolves upon cooling toward $T = 2$ K, where low-field curvature can again be attributed to the small magnetic impurity observed in the temperature-dependent susceptibility data. This impurity is best modeled via a Brillouin function fit with $S = 2$ and a 0.36% molar fraction of impurity moments combined with the linear bulk contribution (Van Vleck plus exchange bound moments) as shown via the fit in the figure. This impurity fraction is consistent with the μ_{eff} value extracted from the Curie term in the $\chi(T)$ data, which translates to a 0.31% molar fraction of $S = 2$ moments.

Looking at lower temperatures, Figure 3c plots AC susceptibility data measured down to $T = 0.1$ K. The real part of the AC susceptibility χ' shows no signatures of a magnetic transition/freezing or frequency dependence between the AC drive frequencies of $f = 524$ Hz and $f = 9984$ Hz. These data exclude low-temperature long-range spin ordering or spin freezing in Ca_3CrN_3 above 100 mK. The ratio of $J/T_{AF} > 3400$ in Ca_3CrN_3 is surprisingly large relative to other reported quantum spin chains. The cuprate chains Sr_2CuO_3 and $SrCuO_2$ exhibit the largest known ratios of $J/T_{AF} \approx 556$[30,58–60] and of $J/T_{AF} \approx 1733$[61–63] in spin chain materials to the best of our knowledge. Other previously studied spin chain compounds show significantly lower J/T_{AF} ratios of ≈ 7 in $NaCu_2O_2$[49] and $J/T_{AF} \approx 12$ in $BaCo_2V_2O_8$.[57]

Theoretical Model and Results

Electronic Structure

To better understand the magnetic exchange in this compound, we performed electronic structure calculations on multiple magnetic configurations to identify the ground state collinear spin order within DFT. The lowest energy spin configuration corresponds to an antiferromagnetic state (AFM1). Spins on CrN_3 units within an (001) plane are ferromagnetically aligned while adjacent planes couple antiferromagnetically (Figure S1). As we show below, this configuration is equivalently described as zig-zag chains, comprising CrN_3 triangles running along c, with antiferromagnetic coupling within the chain and ferromagnetic coupling between chains. The next lowest energy magnetic configuration AFM2 is 1 meV/f.u. higher in energy and exhibits antiferromagnetic coupling of nearest neighbor Cr^{3+} ions along all directions. The fully polarized state with all ferromagnetic interactions is much higher in energy (-19 meV/f.u meV/f.u.), has a local moment of $1.00\,\mu_B$ and is metallic. The projected local magnetic moments and calculated band gaps for the AFM1 and AFM2 structures are almost the same: $m(\mathrm{Cr, AFM1}) = 0.97\,\mu_B$ ($m(\mathrm{Cr, AFM2}) = 0.98\,\mu_B$) and $E_\mathrm{g}^\mathrm{AFM1} = 0.29$ eV ($E_\mathrm{g}^\mathrm{AFM2} = 0.41$ eV). The band gap dependence on the plus U correction shows that electron-electron interactions beyond those captured by PBE are necessary to open a band gap (Figure S4), i.e., Ca_3CrN_3 is semiconducting for $0 < U \leq 3\,\mathrm{eV}$. All values agree with the $S = 1/2$ state and the black appearance of Ca_3CrN_3.

Chemical Bonding

Figure 4 shows the spin-polarized electronic structure of Ca_3CrN_3 with the AFM1 configuration and the PBE+U relaxed crystal structure. The band structure (Figure 4a) and atom projected density of states (DOS, Figure 4b) show that there are three main groups of states in the valence band with different bandwidths and varying degrees of orbital hybridization. Well below the Fermi level, from $-5\,\mathrm{eV}$ to $-3\,\mathrm{eV}$, we find strong Cr $3d$ – N $2p$ σ-bonding

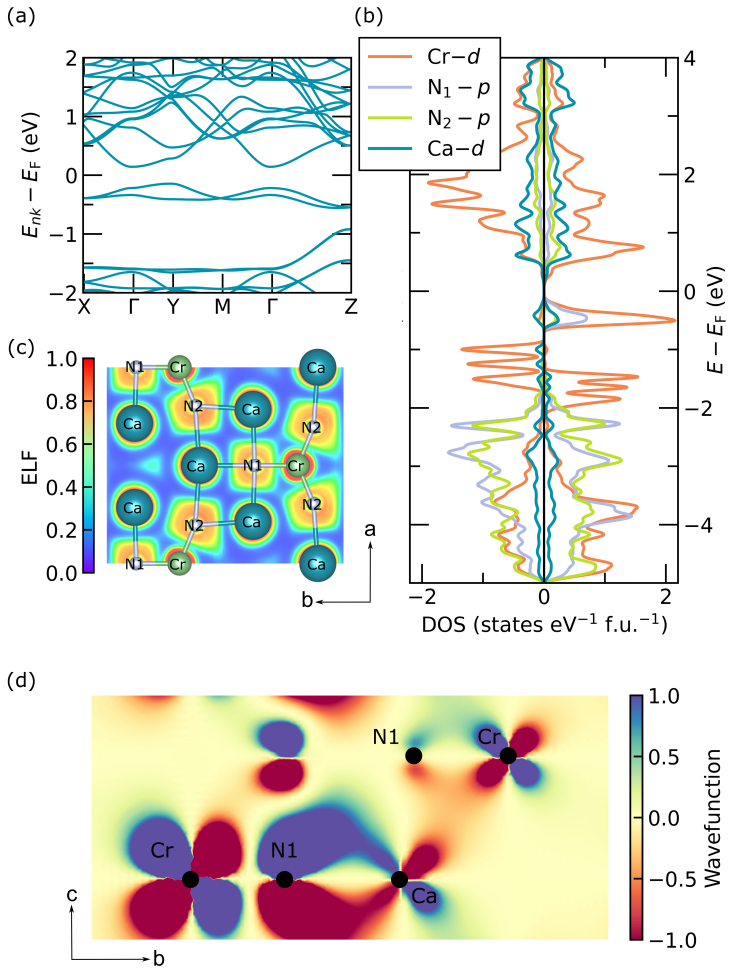

Figure 4: Spin-polarized (a) electronic band structure and (b) density of states (DOS) of Ca_3CrN_3. N1 denotes the nitrogen site contributing to the exchange pathway in Figure 5. N2 corresponds to the nitrido ligands facing away from the chain. (b) Two-dimensional ELF plot in the (001) plane shows perturbations to the spherical bonding environment of the nitrido ligands. (c) Orbital wavefunctions in real space at the Γ point contributing to the described exchange pathway involving Cr d_{yz}, N $2p_z$, and Ca d_{yz} orbitals.

interactions, and large delocalization of the electronic states about the $[CrN_3]^{6-}$ unit (Figure S5). This can be understood as exploiting the $sp^2(x, y)$ hybridization within the N_3 plane (or suitably symmetry adapted molecular orbitals of N $2p$ with C_{2v} symmetry). From approximately -3 to -2 eV, we find additional strong intersite N $2p$ hybridization, which is also evident in the electron localization function (ELF) calculations (Figure 4c). Then from -2.5 to -1.5 eV, there is appreciable hybridization of N1 $2p_z$ orbitals (oriented perpendicular to the triangular N_3 plane) with Ca $3d$ states, which is similar to the covalency found in cubic Ca_3N_2.[64]

The filled antibonding Cr $3d$ states span from -1.5 – -0.5 eV. The majority and minority spin $d_{z^2-r^2}$ π^* orbitals (a_1 symmetry) are filled first followed by the majority spin Cr d_{yz} orbitals (b_1 symmetry) hybridized with N $2p_z$ and Ca $3d$ states. This electron filling and distribution of states can be understood by recognizing that the bonding in the nitridometalate[65] occurs between a strong covalent and complex anion, i.e., $[CrN_3]^{6-}$, and a charged balancing electropositive alkaline earth metal. Because the coordinating nitrido ligands atoms are strong π-donors, in comparison to oxo-ligands, they stabilize the Cr^{3+} low-spin $S = 1/2$ state within the planar isosceles $[CrN_3]^{6-}$. The Cr^{3+} ions (d^3 electronic configuration) adopt the $a_1^2 b_1^1$ electronic configuration (in standard setting for C_{2v} symmetry).

The low-energy d_{yz}-derived band uniquely exhibits low dispersion (~ 0.5 eV, Figure 4a) throughout most of the Brillouin zone (BZ) owing to N $2p_z$ π^* antibonding interaction. The empty N2 $2p_z$ orbital participates in $d\pi - p\pi$ backbonding[66] with the Cr transition metal. This charge transfer and double bond formation makes ternary nitrides distinct from binary main group nitrides.[67] The interaction increases the band dispersions from $\Gamma - Z$ in the BZ (Figure 4a) but there remains isolated and narrow flat bands close to the Fermi level. Such electronic structures are of interest for realizing a range of quantum phenomena[68,69] and its existence in Ca_3CrN_3 suggests strong electron-electron interactions within this manifold coexist with strong covalent metal-ligand interactions within the anionic unit. All other Cr d orbitals are unoccupied in the conduction band.

The differences between the two nitrogen sites shown in Figure 4b are more apparent in the (ELF) calculations, where we find nitrogen site N1 (approximately four coordinate) and N2 (three coordinate) exhibit different chemical bonding environments. The ELF basin about N1 exhibits high electron localization in the (001) plane and a distorted square shape. It is puckered along the Cr-N1 bond, while more covalent interactions are found in the region between Ca and N1 (moderate ELF values). This leads to a longer Cr-N1 bond and shorter Ca-N1 bond length that allows the hybridization shown in the PDOS in the low-energy region. Physically, the larger π delocalization from the nitrido ligands permits the N1 $2p_z$ orbital interaction with the adjacent calcium cation (Ca1) in the next layer, as shown in the real-space wavefunction projection (Figure 4c). As a result, we identify a quasi-1D zig-zag chain network in Ca_3CrN_3 (Figure 5a), which we show below is critical to mediating the magnetic exchange path. (Ca2 does not participate in the magnetic exchange pathway.) Figure 4d shows that the N $2p_z$ orbital transfers electron density into the nominally empty Ca d_{yz} orbitals through both σ and π interactions.

The N2 environment is more asymmetric. Although exhibiting similar bonding interactions, N2 exhibits stronger double bond character (one σ and one π bond) with Cr, leading to the shorter Cr-N2 bond lengths (compared to the Cr-N1 distance) and more ionic interactions with Ca (lower ELF values, longer Ca-N2 distances). This bonding results in nominally one electron lone pair localized in the puckered region of the ELF basin between Cr and N2.

Exchange Interactions

We examine several physical exchange paths involving relevant interatomic distances to identify the microscopic origin of the large, measured $J = 340\,\mathrm{K}$ value. First, the shortest Cr–Cr distance in the compound is $4.73\,\text{Å}$, which eliminates direct exchange as a possible origin. Next, common symmetric superexchange (SE) involves main group ligands L coordinating transition metals M in an extended network. Here Cr–N–Cr SE paths are disconnected, which suggests that typical SE is not dominant. Super-superexchange (SSE) involves an

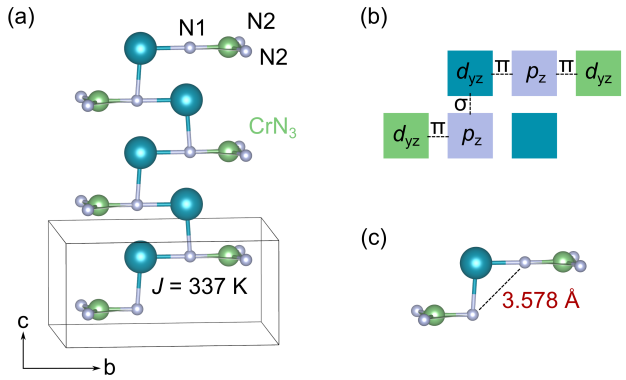

Figure 5: Zig-zag spin-chain motif in Ca_3CrN_3. (a) Super-superexchange pathway through diamagnetic calcium (Cr−N$\cdots$Ca$\cdots$N−Cr) creates a quasi-1D spin chain utilizing the N1 nitrogen site. (b) Orbitals participating in the SSE and the corresponding bonding interactions. (c) The through space SSE Cr−N$\cdots$N−Cr pathway, highlighting that the long N−N distance 3.578 Å, exceeds that required for orbital overlap.

M–$L\cdots L$–M path. Although less common in three-dimensional complex oxides, its strength can be larger than the SE interaction.[70,71] SSE could occur in Ca_3CrN_3 either through space along a $Cr-N\cdots N-Cr$ path or alternatively mediated by diamagnetic calcium as $Cr-N\cdots Ca\cdots N-Cr$ (Figure 5a,b). Through-space interactions have been reported in materials with oxoanions such as phosphates,[72] and in Ca_3CrN_3 would occur through the nitrogen anions.

To address the through space SSE interaction, we determined the shortest N-N distance in the structure is d_{N-N} =3.578 Å (Figure 5c), which is longer than the sum of the van der Waals radii of the nitrogen atoms (3.1 Å). As a result, no direct N $2p$ orbital overlap occurs and the through-space interaction is unlikely. Alternatively, the Ca-mediated SSE path may be active given the large wavefunction extent (Figure 4c) and orbital hybridization (Figure 4b). The experimental Ca1-N1 distance is $d_{Ca-N} = 2.383$ Å within the (001) plane. This distance is shorter than the shortest Ca-N distance in the binary nitride Ca_3N_2 of 2.457 Å.[73] The short distance in combination with the nitrogen π delocalization allows the hybridized Cr d_{yz} – N $2p_z$ orbitals to π bond with the adjacent Ca^{2+} ions, occupying the $4c$ Wyckoff position, in a single (001) plane.

Although the Ca d_{yz} interaction with the N $2p_z$ orbital in the next plane should be

Table 2: Atom distances, angles, and orbital interactions in spin chain exchange pathway.

Atom	**Cr**		**N**		**Ca**		**N**		**Cr**
Interaction		π		σ		π		π	
Spin	Up								Down
Orbital	d_{yz}		p_z		d_{yz}		p_z		d_{yz}
Distance (Å)		1.860		2.383		2.519		1.860	
Angle (°)					93.83		93.83		

nonbonding, the transverse bond has some σ character as the N is displaced along c away from the center of mass of the Ca atom. This is discernible as a deviation from 90 ° in the $\mathrm{N-Ca-N}$ path (Table 2). Thus, electron density is transferred into the nominally empty Ca d_{yz} orbital (Figure 4d) via both σ and π interactions with nearest neighbor nitride anions. Therefore, the SSE occurs through the diamagnetic cation in a through-bond interaction rather than a $\mathrm{N\cdots N}$ (through space interaction). Since the $\mathrm{Cr-N\cdots N-Cr}$ is a weak exchange, the corresponding $\mathrm{Cr-N\cdots Ca\cdots N-Cr}$ becomes strongly AFM. Note that the strong stabilization of the AFM1 state compared to the FM state can be understood as due to spin-assisted covalency[74] in the SSE pathway. The AFM1 state permits the Ca d_{yz} – N1 $2p_z$ hybridization while this interaction is absent in the FM state; however, there is a minor through space N-N bonding in the FM spin configuration even at distance of 3.53 Å within the DFT relaxed structure.

Figure 5b highlights the orbitals and interactions that create the SSE pathway, while Table 2 summarizes the distances between atomic pairs. It is important to note that Ca2 ions occupying the 8g Wyckoff position do not participate in the magnetic exchange mechanism, isolating the described pathway and creating the zig-zag spin chains. To the best of our knowledge, there are few reports in all inorganic compounds of SSE through diamagnetic ions; one example includes iron-based chalcohalides.[75] Thus, the nominally long exchange path can be reconciled by recognizing that Ca_3CrN_3 is a transition metal nitridometallate and that the complex $[CrN_3]^{6-}$ anion is charged balanced by cationic Ca^{2+}. Although a

chemical point of view would purport complex electron transfer to the anion, our simulations support that the interactions with Ca are not fully ionic. The effective superexchange may be interpreted as a standard L–M–L path via a complex ligand $L = [CrN_3]$ with the N^{3-} ions also polarized ($\sim$0.05 μ_B), forming the [CrN_3]–Ca–[CrN_3] path. In this case, the ligand carries the spin density and the cation is the bridge between two neighboring moments. Recently, 2D metal-chlorinate frameworks have been reported with unpaired $S = 1/2$ electron density on the ligands with main group diamagnetic metals mediating the magnetic exchange.[76] This highlights the importance of understanding magnetic exchange not just as local spins – even when the spins are in fact very localized within a band dispersion picture – but as the result of 3D wavefunctions with spatial extent.[77] This finding motivates using chemical substitutions (chemical pressure) or applying hydrostatic pressure to tune the orbital hybridization and strength of the orbital interactions in Ca_3CrN_3.

Our detailed analysis of the exchange mechanism (see SI for derivation of the exchange constant) explains the antiferromagnetic ordering along the 1D zig-zag chain in Ca_3CrN_3. Standard SE, also known as the Kramers-Anderson superexchange,[78,79] treats the exchange coupling between two magnetic ions mediated by an anion, often O^{2-}, with a filled p manifold. Examples are transition metal oxides, where hopping occurs between transition metals M with d^n ($n > 0$) electronic configurations and ligands L with occupied oxygen $2p^6$ orbitals. This leads to an effective superexchange

$$J_{MLM} = -\frac{2t^4}{(U+\Delta)^2}\left(\frac{1}{U} + \frac{1}{U+\Delta}\right) \tag{1}$$

where Δ is the energy difference between the metal d level and the occupied intermediate ligand p level and U is the Coulomb matrix element for electrons on the same M d site.

In contrast, the L-M-L superexchange mechanism describing the [CrN_3]–Ca–[CrN_3] chains is very different: (1) the exchange is between two ligands, not two metals; (2) the two ligands are separated by a metal cation, not an anion; and (3) hopping occurs between the

complex ligand and the unoccupied cation d orbitals, not occupied anion p orbitals. Following a similar procedure described elsewhere,[80] we derived an effective SE interaction for this unconventional L-M-L path:

$$J_{LML} = -\frac{2t^4}{\Delta^2}\left(\frac{1}{U} + \frac{2}{U_d + 2\Delta}\right) . \tag{2}$$

The form for the effective exchange slightly differs from the standard SE given in Equation 1. Here, Δ is the charge transfer energy, i.e., energy difference between the bridging metal d level and the level of the ligand state. U_d and U are the Coulomb matrix elements on the bridging cation site and the ligand sites, respectively. Because the intermediate d states are formally unoccupied while the ligand states are occupied, Δ takes a positive value. This further leads to a negative exchange parameter J_{LML}, favoring antiferromagnetic ordering within the chain. We note for Ca_3CrN_3 that we have simplified Eq. 1 and it requires minor modification to account for the alternating σ and π bonding as hopping between [CrN_3] and Ca is not symmetric. Since these parameters come in pairs in the Hamiltonian, they do not change the sign of the exchange. So as long as the unoccupied Ca-d states are higher in energy than the $[CrN_3]^{6-}$ states, which is the case here, $J_{LML} > 0$, and accounts for the observed antiferromagnetic coupling along spin chain.

Having identified the zig-zag chain shown in Figure 5a as the dominant exchange path, we calculated the magnetic exchange coupling constant J with DFT from energy differences of various magnetic spin configurations, shown in Figure S1, to the following quadratic effective spin Hamiltonian

$$H = -\sum_{ij} J_{ij}\mathbf{S}_i \cdot \mathbf{S}_j = -\sum_{ij} J_{ij}J_{ij}S^2\sigma_i\sigma_j$$

where $S = 1/2$ is the total spin of the ion and σ_i take values of ± 1. We found the intrachain antiferromagnetic coupling is of the order of $J = -19$ meV (220 K). This result is in good agreement with the experimentally determined coupling constant of $J = 340$ K. We additionally identified weak antiferromagnetic interchain interactions on the order of

$J = 1 - 2$ meV that are competing with each other due to the pseudohexagonal geometry of the CrN_3 network (Figure S3). The dependence of our calculated J values with U show weak dispersion with the Hubbard correction (Figure S4). The weak FM interactions arise from a change in the bonding character from one Cr to its nearest neighbor, i.e., an excited state in which the Cr neighbors along the c-axis are antiferromagnetically coupled does not lead to energetic splitting between the bonding-antibonding d_{yz}-derived bands at the Γ point within the same spin channel. The low energy scale and complex Cr–Cr connectivity (Figure S6) are therefore insufficient to establish macroscopic magnetic ordering among the chains. This confirms our picture of short-range antiferromagnetic order within the chains, identifying Ca_3CrN_3 as a quasi-1D spin chain system.

Conclusions

We synthesized Ca_3CrN_3 and examined its magnetic behavior using magnetization, susceptibility, and powder neutron diffraction measurements. A Cr-N$\cdots$Ca$\cdots$N-Cr superexchange pathway is identified, creating zig-zag spin chains parallel to the crystallographic $c-$axis. Consistent with this model, susceptibility data show a high-temperature, broad feature consistent with the onset of quasi-1D antiferromagnetic correlations in this $S = 1/2$ Cr^{3+} compound. Despite the large Cr$-$Cr distance of 4.73 Å, a strong intrachain exchange constant of $J = 340$ K is extracted. The surprisingly strong interaction strength arises as the result of the hybridization within the $[CrN_3]^{6-}$ units (Cr $3d_yz$ and N $2p_z$ π bonding) and covalency with Ca d_{yz} orbitals. This behavior is a consequence of the chemistry of nitridometallates with early transition metals, and positions them at a boundary where strong local correlations and itinerancy coexist. Strikingly, low temperature AC susceptibility measurements exclude macroscopic magnetic ordering to temperatures as low as $T = 0.1$ K, making this compound a model quantum spin chain material, where the ratio $J/T_{AF} > 3400$ is extraordinary among materials known to us. Slight anisotropies in the exchange, for instance, are known to drive

long-range order in antiferromagnetic quantum spin chains.[81–84] Similarly, extended exchange interactions are known to drive local order,[85–87] and even weak interchain coupling results in long-range antiferromagnetism[88–90] The absence of such order or freezing makes Ca_3CrN_3 a near ideal testbed for probing fractionalized, spinon excitations sought for potential far-term quantum computing and spintronic applications and establishes magnetic nitrides as an exciting new frontier for quantum magnetism. In conclusion, we identify Ca_3CrN_3 as a highly quantum spin chain compound where nitrogen-mediated superexchange creates large magnetic coupling within the chains, supporting antiferromagnetic short-range order, while the weak interchain coupling is frustrated from driving long-range magnetic order.

Acknowledgement

J.M.R. thanks K.R. Poeppelmeier for helpful conversations on the chemistry of metal nitrido complexes and nitridometallates. This work was supported by the Air Force Office of Scientific Research under award number FA9550-23-1-0042. The research reported here made use of the shared facilities of the Materials Research Science and Engineering Center (MRSEC) at UC Santa Barbara: NSF DMR–2308708. The UC Santa Barbara MRSEC is a member of the Materials Research Facilities Network (www.mrfn.org). This research used resources at the High Flux Isotope Reactor, a DOE Office of Science User Facility operated by the Oak Ridge National Laboratory. This research was supported in part through the computational resources and staff contributions provided for the Quest high performance computing facility at Northwestern University which is jointly supported by the Office of the Provost, the Office for Research, and Northwestern University Information Technology. R2SCAN calculations were performed using the Department of Defense High-Performance Computing Modernization Program (DOD-HPCMP). This research was supported in part by Lilly Endowment, Inc., through its support for the Indiana University Pervasive Technology Institute, and by Indiana University startup funds.

Supporting Information Available

The Supporting Information is available free of charge at: [***Link to be inserted***]. This information includes crystallographic information, DFT energetics of different spin configurations, schematics of main exchange pathways and various spin configurations, Cr-N σ bonding visualizations, superexchange derivation, and Ca-Ca network.

References

(1) Medarde, M. L. Structural, magnetic and electronic properties of perovskites (R = rare earth). *Journal of Physics: Condensed Matter* **1997**, *9*, 1679, DOI: 10.1088/0953-8984/9/8/003.

(2) Tsurkan, V.; Krug von Nidda, H.-A.; Deisenhofer, J.; Lunkenheimer, P.; Loidl, A. On the complexity of spinels: Magnetic, electronic, and polar ground states. *Physics Reports* **2021**, *926*, 1–86, DOI: 10.1016/j.physrep.2021.04.002.

(3) Xu, Y.; Wang, L. S.; Huang, Y. Y.; Ni, J. M.; Zhao, C. C.; Dai, Y. F.; Pan, B. Y.; Hong, X. C.; Chauhan, P.; Koohpayeh, S. M. et al. Quantum Critical Magnetic Excitations in Spin-1/2 and Spin-1 Chain Systems. *Phys. Rev. X* **2022**, *12*, 021020, DOI: 10.1103/PhysRevX.12.021020.

(4) Rosenberg, E.; Andersen, T. I.; Samajdar, R.; Petukhov, A.; Hoke, J. C.; Abanin, D.; Bengtsson, A.; Drozdov, I. K.; Erickson, C.; Klimov, P. V. et al. Dynamics of magnetization at infinite temperature in a Heisenberg spin chain. *Science* **2024**, *384*, 48–53, DOI: 10.1126/science.adi7877.

(5) Soriano, D.; Katsnelson, M. I.; Fernández-Rossier, J. Magnetic Two-Dimensional Chromium Trihalides: A Theoretical Perspective. *Nano Letters* **2020**, *20*, 6225–6234, DOI: 10.1021/acs.nanolett.0c02381.

(6) Burch, K. S.; Mandrus, D.; Park, J.-G. Magnetism in two-dimensional van der Waals materials. *Nature* **2018**, *563*, 47–52, DOI: 10.1038/s41586-018-0631-z.

(7) Kageyama, H.; Hayashi, K.; Maeda, K.; Attfield, J. P.; Hiroi, Z.; Rondinelli, J. M.; Poeppelmeier, K. R. Expanding frontiers in materials chemistry and physics with multiple anions. *Nature Communications* **2018**, *9*, 772, DOI: 10.1038/s41467-018-02838-4.

(8) Kawamura, F.; Murata, H.; Imura, M.; Yamada, N.; Taniguchi, T. Synthesis of CaSnN2 via a high-pressure metathesis reaction and the properties of II-Sn-N2 (II= Ca, Mg, Zn) semiconductors. *Inorganic Chemistry* **2021**, *60*, 1773–1779.

(9) Kawamura, F.; Imura, M.; Murata, H.; Yamada, N.; Taniguchi, T. Synthesis of a Novel Rocksalt-Type Ternary Nitride Semiconductor MgSnN2 Using the Metathesis Reaction Under High Pressure. *European Journal of Inorganic Chemistry* **2020**, *2020*, 446–451.

(10) Verdier, P.; L'Haridon, P.; Maunaye, M.; Marchand, R. Etude structurale de CaGaN. *Acta Crystallographica Section B: Structural Crystallography and Crystal Chemistry* **1974**, *30*, 226–228.

(11) Juza, R.; Hund, F. Metal amides and metal nitrides. XVII. The ternary nitrides Li3AlN2 and Li3GaN2. *Z. anorg. Chem.* **1948**, *257*, 13–25.

(12) Rom, C. L.; Fallon, M. J.; Wustrow, A.; Prieto, A. L.; Neilson, J. R. Bulk synthesis, structure, and electronic properties of magnesium zirconium nitride solid solutions. *Chemistry of Materials* **2021**, *33*, 5345–5354.

(13) Chern, M. Y.; DiSalvo, F. J. Synthesis, structure, electric, and magnetic properties of CaNiN. *Journal of Solid State Chemistry* **1990**, *88*, 459–464.

(14) Weidemann, M.; Werhahn, D.; Mayer, C.; Kläger, S.; Ritter, C.; Manuel, P.; Attfield, J. P.; Kloß, S. D. High-pressure synthesis of Ruddlesden–Popper nitrides. *Nature Chemistry* **2024**, DOI: 10.1038/s41557-024-01558-1.

(15) Sun, W.; Barterl, C. J.; Arca, E.; Bauers, S. R.; Matthews, B.; Orvananos, B.; Chen, B.-R.; Toney, M. F.; Schelhas, L. T.; Tumas, W. et al. A map of the inorganic ternary metal nitrides. *Nature Materials* **2019**, *18*, 732–739, DOI: 10.1038/s41563-019-0396-2.

(16) Arca, E.; Lany, S.; Perkins, J. D.; Bartel, C.; Mangum, J.; Sun, W.; Holder, A.; Ceder, G.; Gorman, B.; Teeter, G. et al. Redox-mediated stabilization in zinc molybdenum nitrides. *Journal of the American Chemical Society* **2018**, *140*, 4293–4301.

(17) Woods-Robinson, R.; Stevanović, V.; Lany, S.; Heinselman, K. N.; Horton, M. K.; Persson, K. A.; Zakutayev, A. Role of disorder in the synthesis of metastable zinc zirconium nitrides. *Physical Review Materials* **2022**, *6*, 043804.

(18) Talley, K. R.; Perkins, C. L.; Diercks, D. R.; Brennecka, G. L.; Zakutayev, A. Synthesis of $LaWN_3$ nitride perovskite with polar symmetry. *Science* **2021**, *374*, 1488–1491, DOI: 10.1126/science.abm3466.

(19) Trócoli, R.; Frontera, C.; Oró-Solé, J.; Ritter, C.; Alemany, P.; Canadell, E.; Palacín, M. R.; Fontcuberta, J.; Fuertes, A. $MnTa_2N_4$: A Ternary Nitride Spinel with a Strong Magnetic Frustration. *Chemistry of Materials* **2022**, *34*, 6098–6107.

(20) Kautzsch, L.; Georgescu, A. B.; Puggioni, D.; Kent, G.; Taddei, K. M.; Reilly, A.; Seshadri, R.; Rondinelli, J. M.; Wilson, S. D. Canted antiferromagnetism in polar MnSiN 2 with high Néel temperature. *Physical Review Materials* **2023**, *7*, 104406.

(21) King, R. The chemical bonding topology of ternary and quaternary transition metal nitrides containing low-coordinate metal atoms. *Canadian Journal of Chemistry* **1995**, *73*, 963–971, DOI: 10.1139/v95-119.

(22) Chanhom, P.; Fritz, K. E.; Burton, L. A.; Kloppenburg, J.; Filinchuk, Y.; Senyshyn, A.; Wang, M.; Feng, Z.; Insin, N.; Suntivich, J. et al. Sr_3CrN_3: A New Electride with a Partially Filled d-Shell Transition Metal. *Journal of the American Chemical Society* **2019**, *141*, 10595–10598, DOI: 10.1021/jacs.9b03472.

(23) Cordier, G.; Kniep, R.; Höhn, P.; Rabenau, A. Ca6GaN5 und Ca6FeN5. Verbindungen mit [CO3] 2–isosteren Anionen [GaN3] c- und [FeN3] 6-. *Zeitschrift für anorganische und allgemeine Chemie* **1990**, *591*, 58–66.

(24) Vennos, D. A.; Badding, M. E.; DiSalvo, F. J. Synthesis, structure, and properties of a new ternary metal nitride, Ca3CrN3. *Inorganic Chemistry* **1990**, *29*, 4059–4062.

(25) Green, M. T.; Hughbanks, T. Electronic structures of nitridometalates: molecular and extended-chain ions. *Inorganic Chemistry* **1993**, *32*, 5611–5615, DOI: 10.1021/ic00076a031.

(26) Yee, K. A.; Hughbanks, T. Spin state stabilities and distortions of the novel trinitridotransition metalate(6-), (M = vanadium, chromium, iron) ions. *Inorganic Chemistry* **1992**, *31*, 1921–1925, DOI: 10.1021/ic00036a036.

(27) Cao, Y.; Kirsanova, M. A.; Ochi, M.; Al Maksoud, W.; Zhu, T.; Rai, R.; Gao, S.; Tsumori, T.; Kobayashi, S.; Kawaguchi, S. et al. Topochemical synthesis of Ca3CrN3H involving a rotational structural transformation for catalytic ammonia synthesis. *Angewandte Chemie International Edition* **2022**, *61*, e202209187.

(28) Cao, Y.; Toshcheva, E.; Almaksoud, W.; Ahmad, R.; Tsumori, T.; Rai, R.; Tang, Y.; Cavallo, L.; Kageyama, H.; Kobayashi, Y. Ammonia synthesis via an associative mechanism on alkaline earth metal sites of ca3crn3h. *ChemSusChem* **2023**, *16*, e202300234.

(29) Johnston, D. C.; Kremer, R.; Troyer, M.; Wang, X.; Klümper, A.; Bud'ko, S. L.; Panchula, A.; Canfield, P. Thermodynamics of spin S= 1/2 antiferromagnetic uniform and alternating-exchange Heisenberg chains. *Physical Review B* **2000**, *61*, 9558.

(30) Kojima, K.; Fudamoto, Y.; Larkin, M.; Luke, G.; Merrin, J.; Nachumi, B.; Uemura, Y.; Motoyama, N.; Eisaki, H.; Uchida, S. et al. Reduction of ordered moment and Néel temperature of quasi-one-dimensional antiferromagnets Sr_2CuO_3 and Ca_2CuO_3. *Physical review letters* **1997**, *78*, 1787.

(31) He, Z.; Fu, D.; Kyômen, T.; Taniyama, T.; Itoh, M. Crystal growth and magnetic properties of BaCo2V2O8. *Chemistry of materials* **2005**, *17*, 2924–2926.

(32) Luther, A.; Peschel, I. Calculation of critical exponents in two dimensions from quantum field theory in one dimension. *Physical Review B* **1975**, *12*, 3908.

(33) Lake, B.; Tennant, D.; Nagler, S. Novel longitudinal mode in the coupled quantum chain compound KCuF 3. *Physical Review Letters* **2000**, *85*, 832.

(34) Lake, B.; Tennant, D. A.; Frost, C. D.; Nagler, S. E. Quantum criticality and universal scaling of a quantum antiferromagnet. *Nature materials* **2005**, *4*, 329–334.

(35) Schlappa, J.; Kumar, U.; Zhou, K.; Singh, S.; Mourigal, M.; Strocov, V.; Revcolevschi, A.; Patthey, L.; Rønnow, H.; Johnston, S. et al. Probing multi-spinon excitations outside of the two-spinon continuum in the antiferromagnetic spin chain cuprate Sr2CuO3. *Nature communications* **2018**, *9*, 5394.

(36) Zaliznyak, I. A.; Broholm, C.; Kibune, M.; Nohara, M.; Takagi, H. Anisotropic Spin Freezing in the $S = 1/2$ Zigzag Chain Compound $SrCuO_2$. *Phys. Rev. Lett.* **1999**, *83*, 5370–5373, DOI: 10.1103/PhysRevLett.83.5370.

(37) Sachdev, S. Quantum magnetism and criticality. *Nature Physics* **2008**, *4*, 173–185, DOI: 10.1038/nphys894.

(38) Rodríguez-Carvajal, J. Recent advances in magnetic structure determination by neutron powder diffraction. *Physica B: Condensed Matter* **1993**, *192*, 55–69, DOI: https://doi.org/10.1016/0921-4526(93)90108-I.

(39) Giannozzi, P.; Andreussi, O.; Brumme, T.; Bunau, O.; Buongiorno Nardelli, M.; Calandra, M.; Car, R.; Cavazzoni, C.; Ceresoli, D.; Cococcioni, M. et al. Advanced capabilities for materials modelling with Quantum ESPRESSO. *Journal of Physics: Condensed Matter* **2017**, *29*, 465901, DOI: 10.1088/1361-648x/aa8f79.

(40) Perdew, J. P.; Burke, K.; Ernzerhof, M. Generalized Gradient Approximation Made Simple. *Phys. Rev. Lett.* **1996**, *77*, 3865–3868, DOI: 10.1103/PhysRevLett.77.3865.

(41) Perdew, J. P.; Burke, K.; Ernzerhof, M. Generalized Gradient Approximation Made Simple [Phys. Rev. Lett. 77, 3865 (1996)]. *Phys. Rev. Lett.* **1997**, *78*, 1396–1396, DOI: 10.1103/PhysRevLett.78.1396.

(42) Dudarev, S. L.; Botton, G. A.; Savrasov, S. Y.; Humphreys, C. J.; Sutton, A. P. Electron-energy-loss spectra and the structural stability of nickel oxide: An LSDA+U study. *Phys. Rev. B* **1998**, *57*, 1505–1509, DOI: 10.1103/PhysRevB.57.1505.

(43) Garrity, K. F.; Bennett, J. W.; Rabe, K. M.; Vanderbilt, D. Pseudopotentials for high-throughput DFT calculations. *Computational Materials Science* **2014**, *81*, 446–452, DOI: 10.1016/j.commatsci.2013.08.053.

(44) Ködderitzsch, D.; Hergert, W.; Temmerman, W. M.; Szotek, Z.; Ernst, A.; Winter, H. Exchange interactions in NiO and at the NiO(100) surface. *Phys. Rev. B* **2002**, *66*, 064434, DOI: 10.1103/PhysRevB.66.064434.

(45) Logemann, R.; Rudenko, A. N.; Katsnelson, M. I.; Kirilyuk, A. Exchange interactions in transition metal oxides: the role of oxygen spin polarization. *Journal of Physics: Condensed Matter* **2017**, *29*, 335801, DOI: 10.1088/1361-648x/aa7b00.

(46) Dufek, V.; Petrů, F.; Brožek, V. Über Sauerstoff-haltige Verbindungen vom Strukturtyp B1 der ersten vier Übergangsmetalle. *Monatshefte für Chemie und verwandte Teile anderer Wissenschaften* **1967**, *98*, 2424–2430.

(47) Alvarez, S. Bonding and stereochemistry of three-coordinated transition metal compounds. *Coordination Chemistry Reviews* **1999**, *193–195*, 13–41, DOI: 10.1016/s0010-8545(99)00085-5.

(48) Palacios, A. A.; Alemany, P.; Alvarez, S. Electronic Structure and Bonding in Tricoordinate Amido Complexes of Transition Metals. *Inorganic Chemistry* **1999**, *38*, 707–715, DOI: 10.1021/ic980634v.

(49) Capogna, L.; Mayr, M.; Horsch, P.; Raichle, M.; Kremer, R.; Sofin, M.; Maljuk, A.; Jansen, M.; Keimer, B. Helicoidal magnetic order in the spin-chain compound NaCu 2 O 2. *Physical Review B* **2005**, *71*, 140402.

(50) Bonner, J. C.; Fisher, M. E. Linear magnetic chains with anisotropic coupling. *Physical Review* **1964**, *135*, A640.

(51) Estes, W. E.; Gavel, D. P.; Hatfield, W. E.; Hodgson, D. J. Magnetic and structural characterization of dibromo-and dichlorobis (thiazole) copper (II). *Inorganic Chemistry* **1978**, *17*, 1415–1421.

(52) Savina, Y.; Bludov, O.; Pashchenko, V.; Gnatchenko, S.; Lemmens, P.; Berger, H. Magnetic properties of the antiferromagnetic spin-1 2 chain system β-TeVO 4. *Physical Review B—Condensed Matter and Materials Physics* **2011**, *84*, 104447.

(53) Ortiz, B. R.; Sarte, P. M.; Avidor, A. H.; Hay, A.; Kenney, E.; Kolesnikov, A. I.; Pajerowski, D. M.; Aczel, A. A.; Taddei, K. M.; Brown, C. M. et al. Quantum disordered ground state in the triangular-lattice magnet NaRuO2. *Nature Physics* **2023**, *19*, 943–949, DOI: 10.1038/s41567-023-02039-x.

(54) Foner, S. High-Field Antiferromagnetic Resonance in Cr_2O_3. *Phys. Rev.* **1963**, *130*, 183–197, DOI: 10.1103/PhysRev.130.183.

(55) Menth, A.; Remeika, J. P. Magnetic Properties of $(V_{1-x}Cr_x)_2O_3$. *Phys. Rev. B* **1970**, *2*, 3756–3762, DOI: 10.1103/PhysRevB.2.3756.

(56) Sales, B. C.; Wohlleben, D. K. Susceptibility of Interconfiguration-Fluctuation Compounds. *Phys. Rev. Lett.* **1975**, *35*, 1240–1244, DOI: 10.1103/PhysRevLett.35.1240.

(57) Kimura, S.; Takeuchi, T.; Okunishi, K.; Hagiwara, M.; He, Z.; Kindo, K.; Taniyama, T.; Itoh, M. Novel ordering of an S= 1/2 quasi-1d ising-like antiferromagnet in magnetic field. *Physical review letters* **2008**, *100*, 057202.

(58) Ami, T.; Crawford, M.; Harlow, R.; Wang, Z.; Johnston, D.; Huang, Q.; Erwin, R. Magnetic susceptibility and low-temperature structure of the linear chain cuprate Sr 2 CuO 3. *Physical Review B* **1995**, *51*, 5994.

(59) Suzuura, H.; Yasuhara, H.; Furusaki, A.; Nagaosa, N.; Tokura, Y. Singularities in optical spectra of quantum spin chains. *Physical review letters* **1996**, *76*, 2579.

(60) Keren, A.; Le, L.; Luke, G.; Sternlieb, B.; Wu, W.; Uemura, Y.; Tajima, S.; Uchida, S. Muon-spin-rotation measurements in infinite-layer and infinite-chain cuprate antiferromagnets: Ca 0.86 Sr 0.14 CuO 2 and Sr 2 CuO 3. *Physical Review B* **1993**, *48*, 12926.

(61) Motoyama, N.; Eisaki, H.; Uchida, S. Magnetic susceptibility of ideal spin 1/2 Heisenberg antiferromagnetic chain systems, Sr 2 CuO 3 and SrCuO 2. *Physical review letters* **1996**, *76*, 3212.

(62) Matsuda, M.; Katsumata, K.; Kojima, K.; Larkin, M.; Luke, G.; Merrin, J.; Nachumi, B.; Uemura, Y.; Eisaki, H.; Motoyama, N. et al. Magnetic phase transition in the S= zigzag-chain compound SrCuO 2. *Physical Review B* **1997**, *55*, R11953.

(63) Zaliznyak, I.; Broholm, C.; Kibune, M.; Nohara, M.; Takagi, H. Anisotropic spin freezing in the S= 1/2 zigzag chain compound $SrCuO_2$. *Physical Review Letters* **1999**, *83*, 5370.

(64) Höhn, P.; Hoffmann, S.; Hunger, J.; Leoni, S.; Nitsche, F.; Schnelle, W.; Kniep, R. β-Ca_3N_2, a Metastable Nitride in the System Ca–N. *Chemistry – A European Journal* **2009**, *15*, 3419–3425, DOI: 10.1002/chem.200801857.

(65) Höhn, P.; Niewa, R. Nitrides of Non-Main Group Elements. 2017; http://dx.doi.org/10.1002/9783527691036.hsscvol1008.

(66) Jansen, N.; Spiering, H.; Gütlich, P.; Schmidt, P. C.; Eyert, V.; Stahl, D.; Kniep, R.; Kübler, J. Mössbauer Spectroscopy and Electronic Structure Calculations of the Nitridoferrates(III): Li3[FeN2] and Ba3[FeN3]. *Angewandte Chemie International Edition in English* **1992**, *31*, 1624–1626, DOI: https://doi.org/10.1002/anie.199216241.

(67) Bronger, W.; Baranov, A.; Wagner, F. R.; Kniep, R. Atomvolumina und Ladungsverteilungen in Nitridometallaten. *Zeitschrift für anorganische und allgemeine Chemie* **2007**, *633*, 2553–2557, DOI: 10.1002/zaac.200700413.

(68) Leykam, D.; Andreanov, A.; Flach, S. Artificial flat band systems: from lattice models to experiments. *Advances in Physics: X* **2018**, *3*, 1473052, DOI: 10.1080/23746149.2018.1473052.

(69) Leykam, D. Flat bands, sharp physics. *AAPPS Bulletin* **2024**, *34*, DOI: 10.1007/s43673-023-00113-3.

(70) Whangbo, M.-H.; Koo, H.-J.; Dai, D. Spin exchange interactions and magnetic structures of extended magnetic solids with localized spins: theoretical descriptions on formal, quantitative and qualitative levels. *Journal of Solid State Chemistry* **2003**, *176*, 417–481, DOI: 10.1016/s0022-4596(03)00273-1.

(71) Whangbo, M.-H.; Koo, H.-J.; Dai, D.; Jung, D. Interpretation of the Magnetic Structures of Cu2Te2O5X2(X = Cl, Br) and Ca3.1Cu0.9RuO6on the Basis of Electronic Structure Considerations: Cases for Strong Super-Superexchange Interactions Involving Cu2+Ions. *Inorganic Chemistry* **2003**, *42*, 3898–3906, DOI: 10.1021/ic0205511.

(72) Diethrich, T. J.; Gnewuch, S.; Dold, K. G.; Taddei, K. M.; Rodriguez, E. E. Tuning Magnetic Symmetry and Properties in the Olivine Series Li1–xFexMn1–xPO4

through Selective Delithiation. *Chemistry of Materials* **2022**, *34*, 5039–5053, DOI: 10.1021/acs.chemmater.2c00372.

(73) Laurent, Y.; Lang, J.; Le Bihan, M.-T. Structure du nitrure de calcium α. *Acta Crystallographica Section B: Structural Crystallography and Crystal Chemistry* **1968**, *24*, 494–499.

(74) Cammarata, A.; Rondinelli, J. M. Spin-assisted covalent bond mechanism in "charge-ordering" perovskite oxides. *Phys. Rev. B* **2012**, *86*, 195144, DOI: 10.1103/PhysRevB.86.195144.

(75) Zhang, X.; Liu, K.; He, J.-Q.; Wu, H.; Huang, Q.-Z.; Lin, J.-H.; Lu, Z.-Y.; Huang, F.-Q. Antiperovskite Chalco-Halides Ba3(FeS4)Cl, Ba3(FeS4)Br and Ba3(FeSe4)Br with Spin Super-Super Exchange. *Scientific Reports* **2015**, *5*, DOI: 10.1038/srep15910.

(76) Collins, K. A.; Saballos, R. J.; Fataftah, M. S.; Puggioni, D.; Rondinelli, J. M.; Freedman, D. E. Synthetic investigation of competing magnetic interactions in 2D metal–chloranilate radical frameworks. *Chemical Science* **2020**, *11*, 5922–5928, DOI: 10.1039/d0sc01994a.

(77) Yuan, L.-D.; Georgescu, A. B.; Rondinelli, J. M. Nonrelativistic Spin Splitting at the Brillouin Zone Center in Compensated Magnets. *Phys. Rev. Lett.* **2024**, *133*, 216701, DOI: 10.1103/PhysRevLett.133.216701.

(78) Kramers, H. L'interaction Entre les Atomes Magnétogènes dans un Cristal Paramagnétique. *Physica* **1934**, *1*, 182–192, DOI: https://doi.org/10.1016/S0031-8914(34)90023-9.

(79) Anderson, P. W. Antiferromagnetism. Theory of superexchange interaction. *Physical Review* **1950**, *79*, 350.

(80) Koch, E. Exchange mechanisms. *Correlated electrons: from models to materials* **2012**, *2*, 1–31.

(81) Yang, C. N.; Yang, C. P. One-Dimensional Chain of Anisotropic Spin-Spin Interactions. III. Applications. *Phys. Rev.* **1966**, *151*, 258–264, DOI: 10.1103/PhysRev.151.258.

(82) Katsura, S. Statistical Mechanics of the Anisotropic Linear Heisenberg Model. *Phys. Rev.* **1962**, *127*, 1508–1518, DOI: 10.1103/PhysRev.127.1508.

(83) Kurmann, J.; Thomas, H.; Müller, G. Antiferromagnetic long-range order in the anisotropic quantum spin chain. *Physica A: Statistical Mechanics and its Applications* **1982**, *112*, 235–255.

(84) Lieb, E. Two Soluble Models of an Antiferromagnetic Chain. *Ann. Phys., NY* **1961**, *16*, 407.

(85) Majumdar, C. K.; Ghosh, D. K. On Next-Nearest-Neighbor Interaction in Linear Chain. I. *Journal of Mathematical Physics* **1969**, *10*, 1388–1398, DOI: 10.1063/1.1664978.

(86) Inagaki, S.; Fukuyama, H. Spin-Peierls state vs Néel state II. Interchain exchange interaction. *Journal of the Physical Society of Japan* **1983**, *52*, 3620–3629.

(87) Dagotto, E.; Rice, T. Surprises on the way from one-to two-dimensional quantum magnets: The ladder materials. *Science* **1996**, *271*, 618–623.

(88) Bocquet, M. Finite-temperature perturbation theory for quasi-one-dimensional spin-$\frac{1}{2}$ Heisenberg antiferromagnets. *Phys. Rev. B* **2002**, *65*, 184415, DOI: 10.1103/PhysRevB.65.184415.

(89) Scalapino, D. J.; Imry, Y.; Pincus, P. Generalized Ginzburg-Landau theory of pseudo-one-dimensional systems. *Phys. Rev. B* **1975**, *11*, 2042–2048, DOI: 10.1103/PhysRevB.11.2042.

(90) Schulz, H. J. Dynamics of Coupled Quantum Spin Chains. *Phys. Rev. Lett.* **1996**, *77*, 2790–2793, DOI: 10.1103/PhysRevLett.77.2790.

TOC Graphic

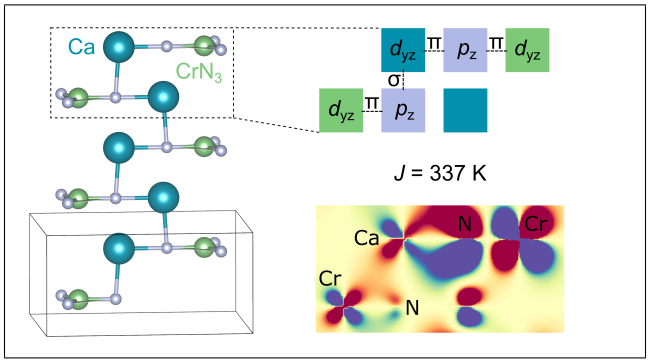

SUPPORTING INFORMATION

Spin Chains with Highly Quantum Character through Strong Covalency in Ca_3CrN_3

Linus Kautzsch,[*,†] Alexandru B. Georgescu,[*,‡] Lin-Ding Yuan,[‡] Keith M. Taddei,[§] Aiden Reilly,[†] Ram Seshadri,[†] James M. Rondinelli,[*,‡] and Stephen D. Wilson[*,†]

†*Materials Department University of California, Santa Barbara 93106, California, United States*

‡*Department of Materials Science and Engineering Northwestern University, Evanston 60208, Illinois, United States*

¶*Department of Chemistry, Indiana University Bloomington 47405, Indiana, United States*

§*Neutron Scattering Division, Oak Ridge National Laboratory Oak Ridge 37831, Tennessee, United States*

||*Department of Chemistry and Biochemistry University of California, Santa Barbara 93106, California, United States*

E-mail: kautzsch@ucsb.edu; georgesc@iu.edu; jrondinelli@northwestern.edu; stephendwilson@ucsb.edu

Contents

1 Magnetic Spin Configurations

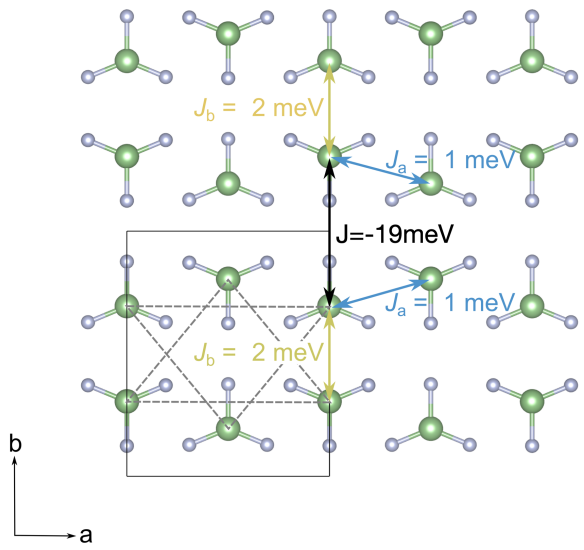

Figure S1: Crystal structure of Ca_3CrN_3 in the ab-plane. $J = -19$ meV is the dominating spin-chain exchange pathway. $J_a = 1$ meV and $J_b = 2$ meV are exchange pathways between chains showing significantly weaker coupling.

We obtain J_a by taking energy differences between magnetic configurations such that a single magnetic coupling interaction changes. Using the magnetic configurations for a single unit cell in Figure S2, we first obtain: $J_a = \frac{E_2 - E_1}{8} = 0.5$ meV. A separate estimate can be obtained from $J_a = \frac{E_3 - E_4}{8} = 1.9$ meV We then estimate that $J_a \approx 1$ meV with an error of 0.5 meV.

Similarly, we obtain two estimates of $J + J_b$, namely $(E_2 - E_3)/4 = -22$ meV and $(E_1 - E_4)/4 = -19.3$ meV. Then, from the supercell calculations in Figure S3 we obtain: $J = ((E'_2 - E'_1) + 4J_a)/4 = -20$ meV. An estimate of J_b can then be obtained from $\frac{E'_3 - E'_2}{4} \approx 2$ meV. Using this value, one could also obtain J from $\frac{E'_1 - E'_3 + 4J_b}{4} = -19$ meV. As a result, we obtain the values presented in the main manuscript and in Figure S1, with an approximate error of 1 meV for J.

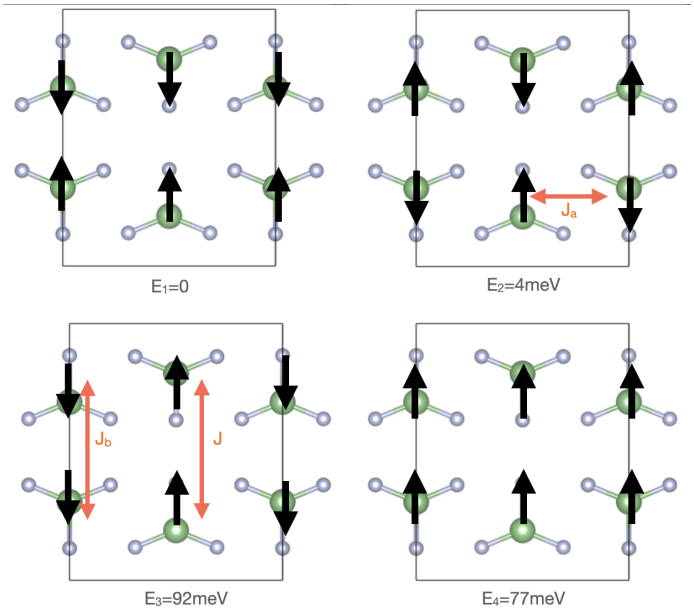

Figure S2: Different spin configurations for a unit cell containing 4 formula units (f.u.) and their relative energies. E_1, E_2, E_3, and E_4, correspond to the AFM1 (DFT ground state), AFM2, AFM3, and FM magnetic configurations, respectively.

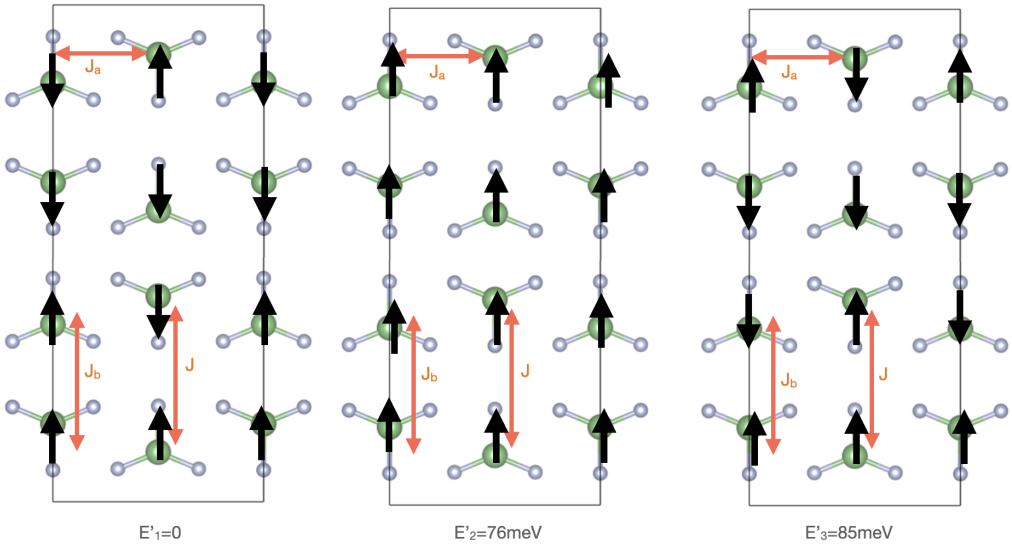

Figure S3: Different spin configurations for a unit cell containing 8 formula units (f.u.) and their relative energies per 4 f.u.

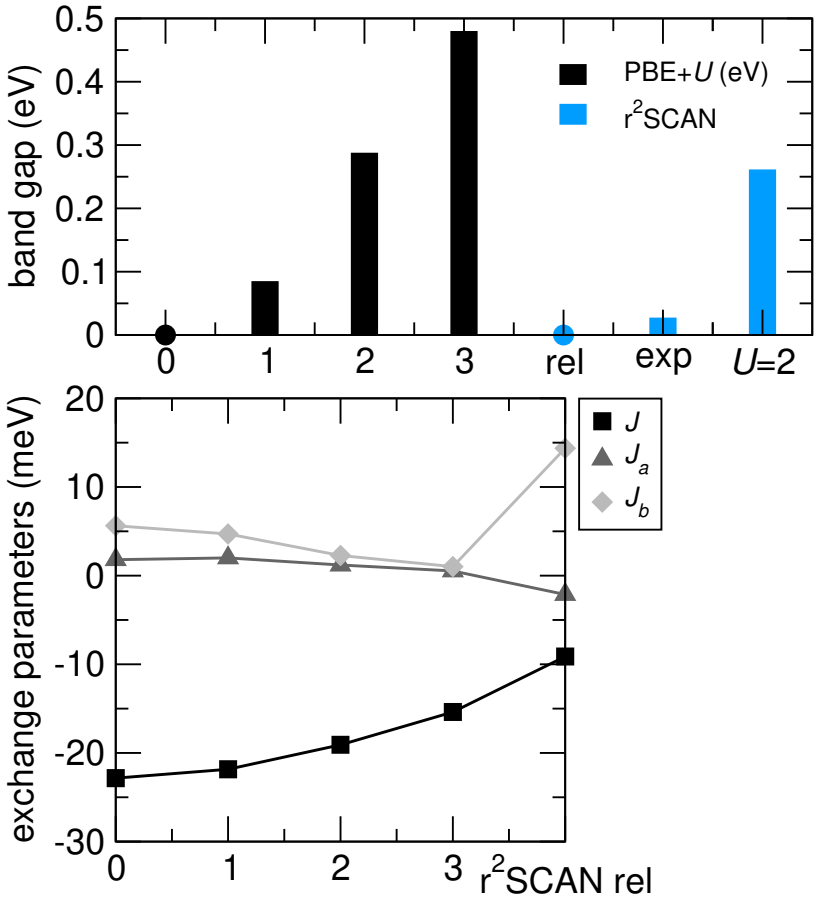

Figure S4: Band gap and J dependence on U for the DFT-PBE+U calculations along with values obtained with the r^{2}SCAN functional. For the latter, a corresponding fully relaxed atomic structure (rel) was obtained with the AFM ground state and used as the r^{2}SCAN reference in the exchange parameter calculations. Additional band gaps were calculated with r^{2}SCAN using the experimental (exp) neutron-diffraction structure and the PBE+U = 2 eV structure. Filled circles indicate a metallic state for the specified exchange-correlation functional.

2 Cr-N Bonding within anionic $[CrN_3]^{6-}$ units

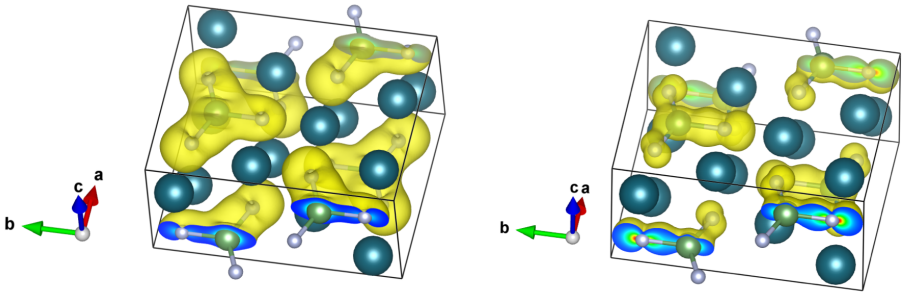

Figure S5: Local density of states (LDOS) plotted in real space, integrated with a Gaussian smearing of 0.05 eV around (left) 4.1 eV below the Fermi level and (right) 3.8 eV below the Fermi level, showing strong Cr-N bonding character.

3 Cr–Cr Network Connectivity

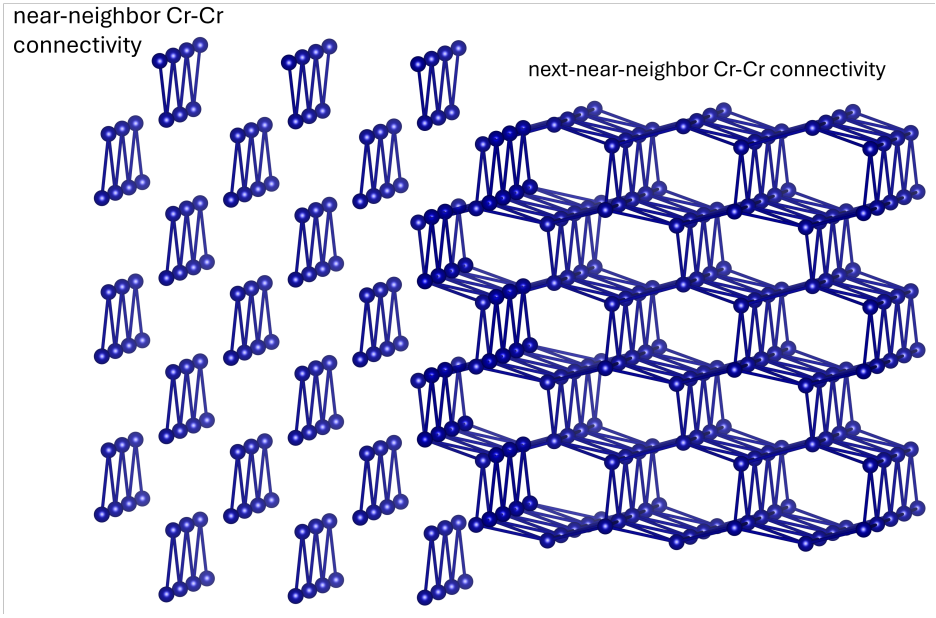

Figure S6: Complex Cr–Cr network connectivity shown through the near-neighbor and next-near neighbor Cr–Cr links.

4 Superexchange through unoccupied d Orbitals

We now examine the exchange between electrons on two magnetic sites i ($i = 1, 2$) mediated by an unoccupied d-orbital to understand the difference between the standard M-L-M SE and the peculiar L-M-L SE (L = ligand). In our model, we consider the hopping between the ligand states on the magnetic site and the intermediate metal d-orbital (t) and the Coulomb repulsion on the two magnetic sites (U) and on the intermediate d-orbital (U_d). We neglect all second nearest neighbor and beyond hopping terms. The Hamiltonian can be written as:

$$H = \sum_{\sigma} \left(\varepsilon_i \sum_i n_{i\sigma} + \varepsilon_d n_{d\sigma} - t \sum_i (c^{\dagger}_{i\sigma} c_{d\sigma} + c^{\dagger}_{d\sigma} c_{i\sigma}) \right) + U \sum_i n_{i\uparrow} n_{i\downarrow} + U_d n_{d\uparrow} n_{d\downarrow} \tag{S1}$$

In the Hilbert space of two electrons with anti aligned spin states occupying the three orbitals, the Hamiltonian matrix is given by:

$$\left|\begin{array}{ccccccccc|l}
0 & 0 & -t & 0 & -t & 0 & 0 & 0 & 0 & c^{\dagger}_{2\uparrow} c^{\dagger}_{1\downarrow} |0\rangle \\
0 & 0 & 0 & -t & 0 & -t & 0 & 0 & 0 & c^{\dagger}_{2\downarrow} c^{\dagger}_{1\uparrow} |0\rangle \\
-t & 0 & \Delta & 0 & 0 & 0 & 0 & t & t & c^{\dagger}_{2\uparrow} c^{\dagger}_{d\downarrow} |0\rangle \\
0 & \text{-t} & 0 & \Delta & 0 & 0 & 0 & -t & -t & c^{\dagger}_{2\downarrow} c^{\dagger}_{d\uparrow} |0\rangle \\
-t & 0 & 0 & 0 & \Delta & 0 & t & 0 & t & c^{\dagger}_{d\uparrow} c^{\dagger}_{1\downarrow} |0\rangle \\
0 & -t & 0 & 0 & 0 & \Delta & -t & 0 & -t & c^{\dagger}_{d\downarrow} c^{\dagger}_{1\uparrow} |0\rangle \\
0 & 0 & 0 & 0 & t & -t & U & 0 & 0 & c^{\dagger}_{1\downarrow} c^{\dagger}_{1\uparrow} |0\rangle \\
0 & 0 & t & -t & 0 & 0 & 0 & U & 0 & c^{\dagger}_{2\downarrow} c^{\dagger}_{2\uparrow} |0\rangle \\
0 & 0 & t & -t & t & -t & 0 & 0 & U_d + 2\Delta & c^{\dagger}_{d\downarrow} c^{\dagger}_{d\uparrow} |0\rangle
\end{array}\right|$$

Downfolding the high energy states into the subspace spanned by the first two states, $c^{\dagger}_{2\uparrow} c^{\dagger}_{d\downarrow} |0\rangle$ and $c^{\dagger}_{2\downarrow} c^{\dagger}_{d\uparrow} |0\rangle$, setting $\varepsilon = 0$, and expanding in $1/U$ leads to:

$$\begin{aligned}
H_{\text{eff}} &= H_{00} + T_{01} \left(\varepsilon - \left(H_{11} + T_{12} \left(\varepsilon - H_{22} \right)^{-1} T_{21} \right) \right)^{-1} T_{10} \\
&\approx H_{00} - T_{01} H_{11}^{-1} T_{10} - T_{01} H_{11}^{-1} T_{12} H_{22}^{-1} T_{21} H_{11}^{-1} T_{10} \\
&= -\frac{2t^2}{\Delta} \begin{pmatrix} 1 & 0 \\ 0 & 1 \end{pmatrix} - \frac{2t^4}{\Delta^2} \left(\frac{1}{U} + \frac{2}{U_d + 2\Delta} \right) \begin{pmatrix} 1 & -1 \\ -1 & 1 \end{pmatrix}.
\end{aligned} \tag{S2}$$

Here, $c^\dagger$ and c are the electron creation and annihilation operators; Δ is defined as the energy difference between the unoccupied intermediate metal d level and the occupied level of the ligand spin state, i.e., $\Delta = \varepsilon_d - \varepsilon_i$. We can rewrite the second term in the second quantized form:

$$H_{ex} = J_{LML}\left(c^\dagger_{2\uparrow}c^\dagger_{1\downarrow}c_{1\downarrow}c_{2\uparrow} - c^\dagger_{2\downarrow}c^\dagger_{1\uparrow}c_{1\downarrow}c_{2\uparrow} - c^\dagger_{2\uparrow}c^\dagger_{1\downarrow}c_{1\uparrow}c_{2\downarrow} + c^\dagger_{2\downarrow}c^\dagger_{1\uparrow}c_{1\uparrow}c_{2\downarrow}\right) \tag{S3}$$

in which

$$J_{LML} = -\frac{2t^4}{\Delta^2}\left(\frac{1}{U} + \frac{2}{U_d + 2\Delta}\right). \tag{S4}$$

Using the identities that $S^x_i = \frac{1}{2}(c^\dagger_{i\uparrow}c_{i\downarrow} + c^\dagger_{i\downarrow}c_{i\uparrow})$, $S^y_i = -\frac{i}{2}(c^\dagger_{i\uparrow}c_{i\downarrow} - c^\dagger_{i\downarrow}c_{i\uparrow})$, $S^z_i = \frac{1}{2}(c^\dagger_{i\uparrow}c_{i\uparrow} - c^\dagger_{i\downarrow}c_{i\downarrow})$, Eq. S3 can be further written in terms of the spin operators for the d orbitals.

$$H_{ex} = -J_{LML}\left(\vec{S}_1 \cdot \vec{S}_2 - \frac{n_1 n_2}{4}\right) \tag{S5}$$

We find that J_{LML} is the effective exchange between the spins at the two adjacent ligand sites and represents the L-M-L superexchange. In comparison, standard M-L-M SE through a doubly occupied p, derived from a similar treatment,[1] takes a slightly different form:

$$J_{MLM} = -\frac{2t^4}{(U+\Delta)^2}\left(\frac{1}{U} + \frac{1}{U+\Delta}\right), \tag{S6}$$

where in this case, Δ is the energy difference between the metal d level and the occupied intermediate ligand p level, that is $\Delta = \varepsilon_i - \varepsilon_p$.

5 r^{2}SCAN Simulation Details and Results

The Strongly Constrained and Appropriately Normed (SCAN) semilocal density functional is known to give a reliable description of common transition metals compounds without the trouble of ascertaining an optimzal plus Hubbard U value.[2] To assess our DFT+U results, we performed additional calculations with the r^{2}SCAN functional[3] as implemented in the Vienna Ab Initio

Simulation Package (VASP)[4,5] using the projector augmented-wave pseudopotential[6] plane-wave methods. The cutoff energies for the plane-wave basis were set to 520 eV for structural relaxations and static total energy calculations. Atomic relaxations were performed until the internal forces were smaller than 0.01 eV Å^{-1}. We employed Γ-centered k-meshes of size $4\times3\times7$ for the primitive cell calculations.

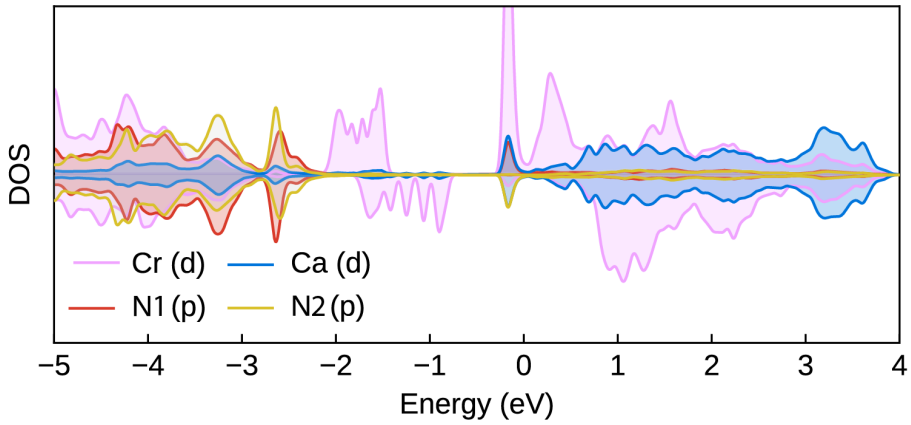

Figure S7: DFT-r^{2}SCAN spin-polarized density of states (DOS) of Ca_3CrN_3 for the fully relaxed r^{2}SCAN crystal structure.

References

(1) Koch, E. Exchange mechanisms. *Correlated electrons: from models to materials* **2012**, *2*, 1–31.

(2) Sun, J.; Ruzsinszky, A.; Perdew, J. P. Strongly Constrained and Appropriately Normed Semilocal Density Functional. *Phys. Rev. Lett.* **2015**, *115*, 036402, DOI: 10.1103/PhysRevLett.115.036402.

(3) Furness, J. W.; Kaplan, A. D.; Ning, J.; Perdew, J. P.; Sun, J. Accurate and Numerically Efficient r2SCAN Meta-Generalized Gradient Approximation. *The Journal of Physical Chemistry Letters* **2020**, *11*, 8208–8215, DOI: 10.1021/acs.jpclett.0c02405, PMID: 32876454.

(4) Kresse, G.; Furthmüller, J. Efficiency of ab-initio total energy calculations for metals and

semiconductors using a plane-wave basis set. *Computational Materials Science* **1996**, *6*, 15–50, DOI: https://doi.org/10.1016/0927-0256(96)00008-0.

(5) Kresse, G.; Furthmüller, J. Efficient iterative schemes for ab initio total-energy calculations using a plane-wave basis set. *Phys. Rev. B* **1996**, *54*, 11169–11186, DOI: 10.1103/PhysRevB.54.11169.

(6) Kresse, G.; Joubert, D. From ultrasoft pseudopotentials to the projector augmented-wave method. *Phys. Rev. B* **1999**, *59*, 1758–1775, DOI: 10.1103/PhysRevB.59.1758.